JACS
JOURNAL OF THE AMERICAN CHEMICAL SOCIETY
pubs.acs.org/JACS

Open Access
This article is licensed under CC-BY 4.0

Article

Activation of Anionic Redox for Stoichiometric and Li-Excess Metal Sulfides through Structural Disordering: Joint Experimental and Theoretical Study

Miyuki Shinoda, Koki Matsunoshita, Masanobu Nakayama, Satoshi Hiroi, Koji Ohara, Masaki Abe, Nozomu Ishiguro, Yukio Takahashi, Gen Hasegawa, Naoaki Kuwata, Tsukasa Iwama, Takuya Masuda, Kosuke Suzuki, Hirofumi Ishii, Yu-Cheng Shao, Daisuke Shibata, Akinori Irizawa, Toshiaki Ohta, Itsuki Konuma, Teppei Ohno, Yosuke Ugata, and Naoaki Yabuuchi*

Cite This: J. Am. Chem. Soc. 2025, 147, 26238−26253

Read Online

ACCESS | Metrics & More | Article Recommendations | Supporting Information

ABSTRACT: Extensive research efforts have been dedicated to Li-excess compounds with anionic redox reaction as potential high-capacity positive electrode materials for Li-ion battery applications. The origin of activation on anionic redox is still under debate, and a unified understanding is necessary, especially for sulfide-based compounds without conductive d electrons. Herein, joint experimental and theoretical study is conducted for Li-excess and stoichiometric compounds with different crystal structures, cation-disordered rocksalt, and cation-ordered layered structures. In contrast to the understanding of Li-excess oxides, sulfide-based compounds with ordered layered structures are electrochemically less active compared with the materials with disordered structure. Theoretical study reveals that a unique local structure for a sulfide ion coordinated by 6 Li ions, SLi_6 configuration, is formed, which can be found only for the disordered structure and not for the layered structure. The unique local structure triggers electron delocalization for sulfide 3p orbitals, leading to superior electronic conductivity, as experimentally evidenced, and thus anionic redox is successfully activated. Furthermore, such nonuniform local structures lead to easier structural distortion and efficient S−S dimerization, and even trimerization (S_3^{2-}), upon delithiation. Although sulfide-based compounds as battery electrode materials suffer from dissolution after oxidation, this practical problem is effectively mitigated by the use of highly concentrated electrolyte solutions with fewer free solvent molecules, leading to superior reversibility for anionic redox. The insights derived can guide the development of high-energy electrode materials with anionic redox with or without transition metal ions possessing conductive d electrons.

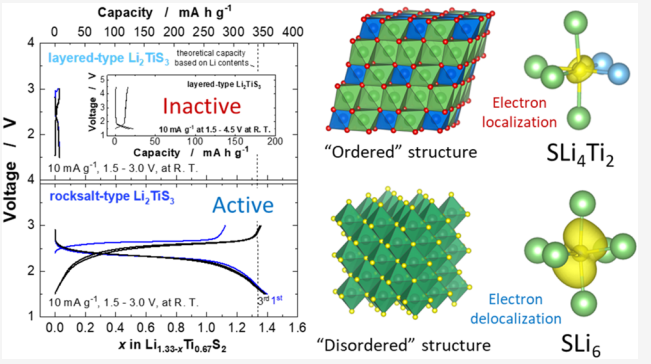

INTRODUCTION

Technological progress on rechargeable batteries is indispensable toward sustainable energy development and fossil fuel-free society. The research achievements on rechargeable batteries successfully resulted in the electrification of automobiles, and the market of electric vehicles is rapidly growing in the world. Currently, Ni-enriched layered materials, $LiNi_{1-2x}Co_xMn_xO_2$, are widely used for batteries in state-of-the-art electric vehicles. Reversible capacities of 170−220 mA h g^{-1} with excellent cyclability are obtained using redox reaction of cationic species, $Ni^{2+}/Ni^{3+}/Ni^{4+}$, Co^{3+}/Co^{4+}.[1,2] Recently, the electrode reversibility of Co-free $LiNiO_2$ has been effectively improved through the engineering of structural defects coupled with surface stabilization.[3,4] Nevertheless, cost-effective and Ni-/Co-free electrode materials are necessary to further accelerate this movement in automobile applications. Lithium-excess and manganese-based electrode materials, Li_2MnO_3 ($Li_{4/3}Mn_{2/3}O_2$) and its derivatives, were extensively studied in the past decade. The enrichment of Li-ion fractions in the host structure leads to higher theoretical capacity as electrode materials. Large reversible capacities are delivered for these electrode materials through the activation of anionic redox reaction, namely, charge compensation by oxide ions on oxidation.[5−8] The emerging new chemistry, anionic redox, potentially boosts the energy density of Li-ion batteries. Nevertheless, the reversibility of anionic redox for oxide ions is not high enough associated with gradual oxygen loss for

Received: March 7, 2025
Revised: June 28, 2025
Accepted: June 30, 2025
Published: July 15, 2025

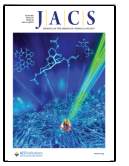

Downloaded via NATL INST FOR MATLS SCIENCE (NIMS) on July 31, 2025 at 02:00:28 (UTC).
See https://pubs.acs.org/sharingguidelines for options on how to legitimately share published articles.

© 2025 The Authors. Published by American Chemical Society

continuous cycles and thus hinders its use for practical applications.

Recently, this concept of anionic redox for Li-excess electrode materials is extended to sulfide ions, which are soft and easily polarizable ions compared with hard oxide ions. Historically, Li_2FeS_2 was studied in 1987 as electrode material and recently revisited as a model electrode material. Both cationic (Fe^{2+}/Fe^{3+}) and anionic ($2S^{2-}/S_2^{2-}$) redox are activated in $Li_{2-x}FeS_2$, and reversible dimer formation of sulfur species proceeds on electrochemical oxidation and lithium removal.[9] Recently, Li_2TiS_3 polymorphs and its derivatives have also been proposed as a new series of Li-excess sulfide system.[10−13] Li_2TiS_3 polymorphs show the unique electrode performance, and Li_2TiS_3 with the cation-disordered rocksalt structure delivers a high-reversible capacity of over 300 mA h g^{-1} by using sulfur-based anionic redox coupled with the percolative Li-ion migration. In contrast, surprisingly, Li_2TiS_3 with the layered structure is electrochemically inactive.[12] Ordered Li_3NbS_4 is also inactive as electrode materials, but a disordered phase shows good electrode reversibility.[14] Similarly, $LiMn_{0.5}Ti_{0.5}S_2$ with the rocksalt structure shows better performance when compared with the sample with the layered structure.[15] This trend, better reversibility for samples with the rocksalt structure, is clearly different from that of $LiCoO_2$, which is the most widely used layered oxide for battery applications. Cation-ordered and layered $LiCoO_2$ shows excellent electrode reversibility, while cation-disordered $LiCoO_2$ shows inferior performance as electrode materials.[16] Electrode reversibility of layered Li_2TiS_3 is also activated when solid solution phases are formed, for instance, Li_2TiS_3−$LiTiS_2$ and Li_2TiS_3−$LiFe_{0.5}Ti_{0.5}S_2$ binary systems.[12] Anion substitution is also proposed to activate electrode reversibility, *i.e.*, $Li_2TiS_{3-x}Se_x$.[17] Nevertheless, the origin of activation of the anionic redox for Li-excess sulfide-based materials is under debate. For battery applications, many sulfides are studied for solid electrolyte and these compounds are designed with main-group elements, e.g., Li_3PS_4, $Li_{10}GeP_2S_{12}$, Li_6PS_5Cl, *etc.* Transition metal ions are eliminated from these compounds used for solid electrolytes because transition metal ions contain conductive d-electrons. The solid electrolyte is ideally required to be a pure ionic conductor and an electronic insulator. In addition, sulfide ions have a reductive nature, and transition metal ions with higher oxidation states are easily reduced by sulfide ions. Therefore, only limited transition metal ions are used for the material synthesis, and there are relatively few studies on sulfide-based compounds with transition metal ions.

In this study, systematic studies on Li_2TiS_3 with different structures are conducted through joint experimental and theoretical approaches. For comparison, non-Li-excess and stoichiometric system, *i.e.*, rocksalt $LiMn_{1/2}Ti_{1/2}S_2$,[15] is also synthesized and characterized, and these results are compared with those of Li_2TiS_3 ($Li_{4/3}Ti_{2/3}S_2$). These electrode materials deliver large reversible capacity, which nearly corresponds to theoretical capacities based on Li contents with solely anionic redox, which cannot be achieved for oxide-based layered compounds. From these results, the factors affecting sulfur-based anionic redox and electrode reversibility are discussed, through which the feasibility of Li-excess metal sulfides for potential battery applications is also evaluated.

EXPERIMENTAL SECTION

Synthesis of Materials. Li_2TiS_3 and $LiMn_{0.5}Ti_{0.5}S_2$ with a disordered structure were synthesized from Li_2S (Sigma-Aldrich), TiS_2 (Sigma-Aldrich), and MnS (Sigma-Aldrich) by mechanical milling using a planetary ball mill (PULVERISETTE 7; FRITSCH) with a ZrO_2 pot (45 mL) and balls at 600 rpm for 12 h. The samples were handled in an Ar-filled glovebox to avoid contact with moisture. Structural evolutions of the samples by milling were studied using an X-ray diffractometer (D2 PHASER, Bruker) equipped with a high-speed one-dimensional detector using Cu Kα radiation generated at 300 W (30 kV and 10 mA) with a Ni filter.

Electrochemical Characterization. Composite positive electrodes composed of 80 wt % Li_2TiS_3 or $LiMn_{0.5}Ti_{0.5}S_2$, 10 wt % acetylene black, and 10 wt % polyvinylidene fluoride (KF 1100; Kureha Co. Ltd.) were dispersed in *N*-methylpyrrolidone and pasted on aluminum foil as a current collector. The electrodes were dried at 120 °C for 2 h in a vacuum. Metallic lithium (Honjo Metal Co., Ltd.) was used as a negative electrode. The electrolyte solution used was 1.0 mol dm^{-3} $LiPF_6$ dissolved in ethylene carbonate/dimethyl carbonate (3:7 by volume, battery grade; Kishida Chemical Co. Ltd.) and 7.25 mol kg^{-1} $LiBF_4$ dissolved in propylene carbonate (battery grade; Kishida Chemical Co. Ltd). A porous polyolefin membrane was used as a separator for the $LiPF_6$ electrolyte, and a glass filter (GB-100R, Advantec) was used as a separator for 7.25 mol kg^{-1} $LiBF_4$ electrolyte with high viscosity. Two-electrode cells (TJ-AC; Tomcell) were assembled in an Ar-filled glovebox.

Materials Characterization. Particle morphology of the samples was observed by using a scanning electron microscope equipped with an energy dispersive X-ray spectrometer (SEM-EDS) (JCM-6000, JEOL). *In situ* XRD data were collected with a battery cell equipped with a Be window combined with an X-ray diffractometer (D8 ADVANCE; Bruker Corp., Ltd.). Soft X-ray absorption spectroscopy (XAS) data were collected at BL-13 (S K-edge and Ti K-edge) in the synchrotron facility of Ritsumeikan University (Synchrotron Radiation Center). Absorption spectra were acquired using the fluorescence yield mode. Hard XAS spectra at the Mn K-edge were collected at beamline BL-12C of the Photon Factory Synchrotron Source in Japan. X-ray total scattering measurements were performed at two beamlines in SPring-8, Japan, to study the local structure by pair distribution function (PDF) analysis. An incident X-ray energy of E = 61.3 keV was used at BL04B2 beamline with hybrid detectors of Ge and CdTe. Measurements were conducted using a two-dimensional CdTe detector (Eiger2 4M) with an incident X-ray energy of 67.0 keV at the BL12B2 beamline. The reduced PDF $G(r)$ was obtained by the conventional Fourier transform of $S(Q)$.[18] The local structure around Li was evaluated by ^{7}Li magic angle spinning nuclear magnetic resonance (MAS NMR) using an ECA-400 spectrometer (JEOL Ltd., Japan). The resonance frequency of the ^{7}Li nucleus was 155.4 MHz. A 1.0 mol dm^{-3} LiCl aqueous solution was used as the chemical shift reference at 0 ppm. A 3.2 mm MAS probe (HXMAS probe; JEOL) and a 3.2 mm zirconia sample tube were used. The MAS spinning rate was varied between 0 and 20 kHz. The width of the $\pi/2$ pulse was 2.8 μs. The pulse-recycling period was kept longer than 17 s to confirm the spin recovering. The NMR spectra were obtained by an MAS-rotation synchronized spin−echo pulse sequence. Hard X-ray photoelectron spectroscopy (HAXPES) measurements were carried out using a custom-made system equipped with a Cr Kα (5414.9 eV) focused X-ray source (Ulvac-Phi) operating at 50 W and an EW-4000 electron analyzer (Scienta Omicron). The incident angle of X-rays and takeoff angle of photoelectrons were fixed at 75 and 75°, respectively. The energy of the photoelectrons passing through the analyzer (pass energy) was fixed at 200 eV. The vacuum pressure in the analysis chamber was ~2 × 10^{-9} mbar. This system was directly attached to an Ar-filled glovebox, so that the samples can be directly transferred to the analysis chamber without exposure to open air. Magnetization measurements for $Li_{2-x}TiS_3$ were performed by using a superconducting quantum interference device (SQUID) magnetometer (MPMS5-SW, Quantum Design, Inc.). The magnetizations for

https://doi.org/10.1021/jacs.5c04018
J. Am. Chem. Soc. 2025, 147, 26238−26253

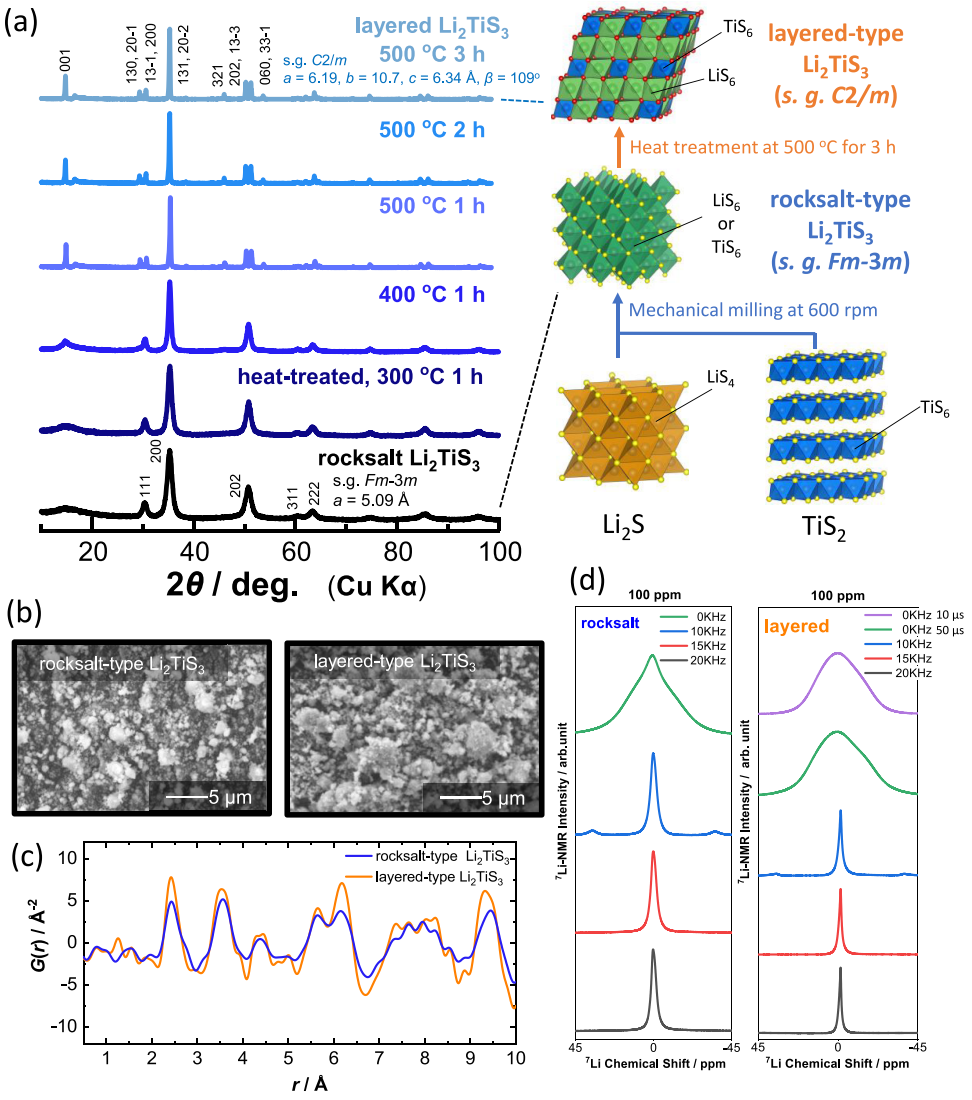

Figure 1. Synthesis and structural characterization of Li_2TiS_3 with ordered and disordered structures: (a) structural evolution of cation-ordered layered Li_2TiS_3 from cation-disordered rocksalt Li_2TiS_3 on heating, and a scheme of material synthesis is also shown. Comparison of (b) SEM images, (c) pair distribution functions, and (d) ^{7}Li NMR spectra of ordered (layered) and disordered (rocksalt) Li_2TiS_3.

all samples were measured by changing the sample temperature from 300 to 12 K under a constant magnetic field of 1000 Oe.

Density Functional Theory Calculations. First-principles calculations based on density functional theory (DFT) for $Li_2(1-x)TiS_3$ system were performed using Vienna Ab initio Simulation Package (VASP)[19,20] with modified Perdew–Burke–Ernzerhof generalized gradient approximation (PBEsol-GGA)[21,22] and with the projector-augmented wave (PAW) method.[23] Cutoff was set as 500 eV, and the *k*-point meshes were sampled such that the product of the meshes and atoms was approximately 600.

RESULTS AND DISCUSSION

Synthesis and Characterization of Rocksalt and Layered Li_2TiS_3. Li-excess titanium sulfide, Li_2TiS_3, was synthesized from a mixture of Li_2S and TiS_2 by high-energy mechanical milling. X-ray diffraction (XRD) patterns of the samples before and after milling are compared in Supporting Figure S1. After mechanical milling, diffraction lines for starting materials disappear and a low-crystallinity sample with cation-disordered rocksalt sulfide is formed. Nanosized materials synthesized by mechanical milling generally consist of agglomerated nanosized grains (~10 nm size) with enriched grain boundaries.[24,25] This rocksalt sulfide is a metastable phase, and after heat treatment at 500 °C for 3 h, a layered sulfide with high crystallinity is obtained. Structural evolution from the rocksalt to layered phase on heating is observed in Figure 1a. The metastable rocksalt phase is stable after heating at 300 °C. Partial crystallization of the layered phase is evidenced after heating at 400 °C, and a small 001 diffraction line is observed for the sample heated at 400 °C. The layered phase with high crystallinity is immediately formed after heating at 500 °C. A superlattice line is also observed at 16.5°, indicating the presence of honeycomb-type in-plane cation ordering for Li and Ti ions. The particle morphology of the sample observed by using a scanning electron microscope (SEM) is also shown in Figure 1b. The increase in particle size after heat treatment is found in SEM images, and Brunauer–Emmett–Teller (BET) measurement reveals that the specific surface area is reduced from 18.1 to 4.3 $m^2\ g^{-1}$ after heat treatment. A similar trend, crystallization of a layered phase from disordered rocksalt phase by heating, is observed in stoichiometric $LiMn_{0.5}Ti_{0.5}S_2$ as reported in the literature.[15] Local structures of rocksalt and layered Li_2TiS_3 have been

https://doi.org/10.1021/jacs.5c04018
J. Am. Chem. Soc. 2025, 147, 26238–26253

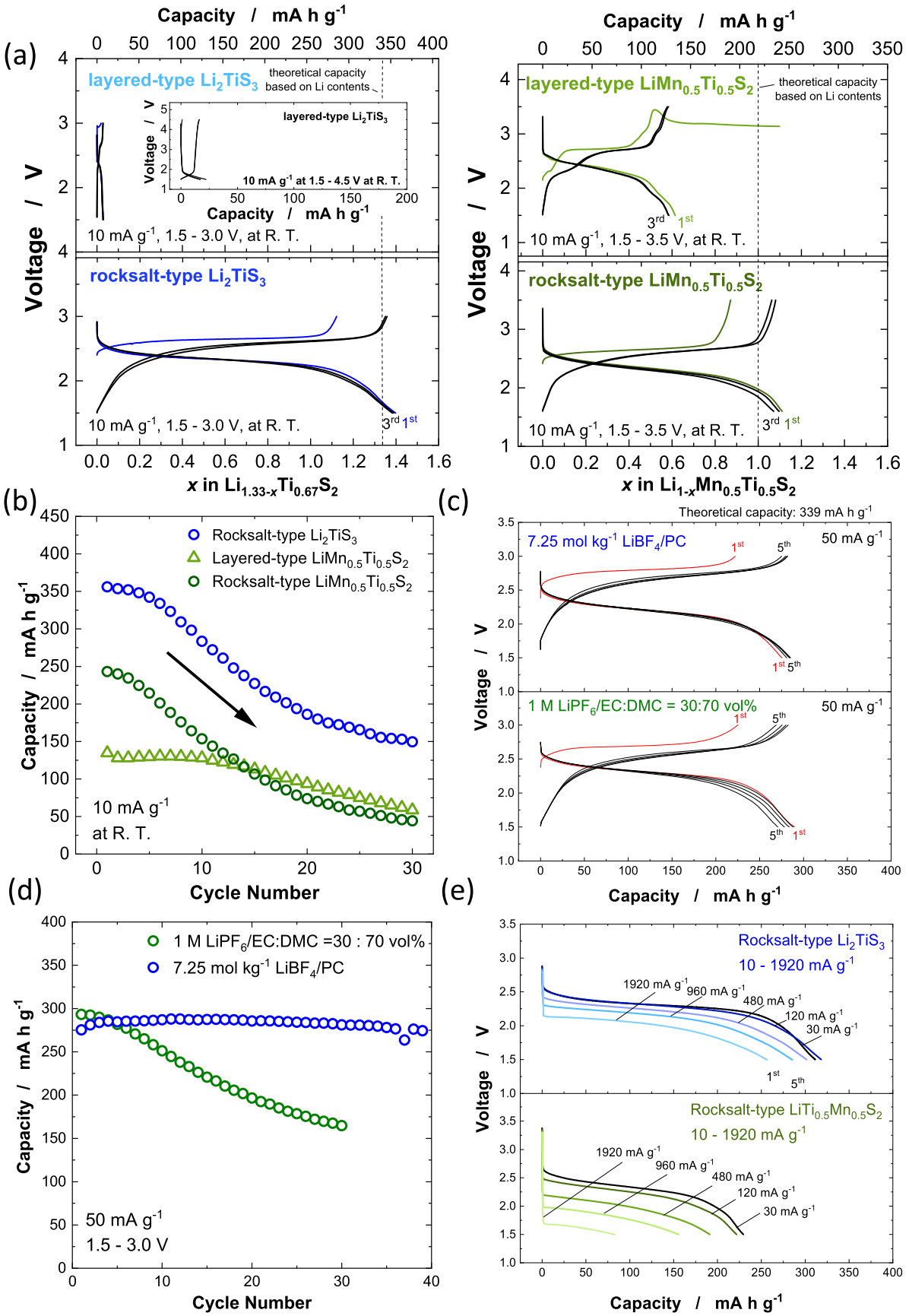

Figure 2. Electrochemical properties of Li-excess and stoichiometric Li sulfides: (a) Galvanostatic charge/discharge curves and (b) capacity retention of ordered (layered) and disordered (rocksalt) Li_2TiS_3 and $LiMn_{0.5}Ti_{0.5}S_2$. Galvanostatic charge/discharge curves and capacity retention with different electrolyte solutions are also shown in (c) and (d), respectively. (e) Comparison of rate capability of disordered (rocksalt) Li_2TiS_3 and $LiMn_{0.5}Ti_{0.5}S_2$ with a mass loading of 4−6 mg cm^{-2}.

https://doi.org/10.1021/jacs.5c04018
J. Am. Chem. Soc. 2025, 147, 26238−26253

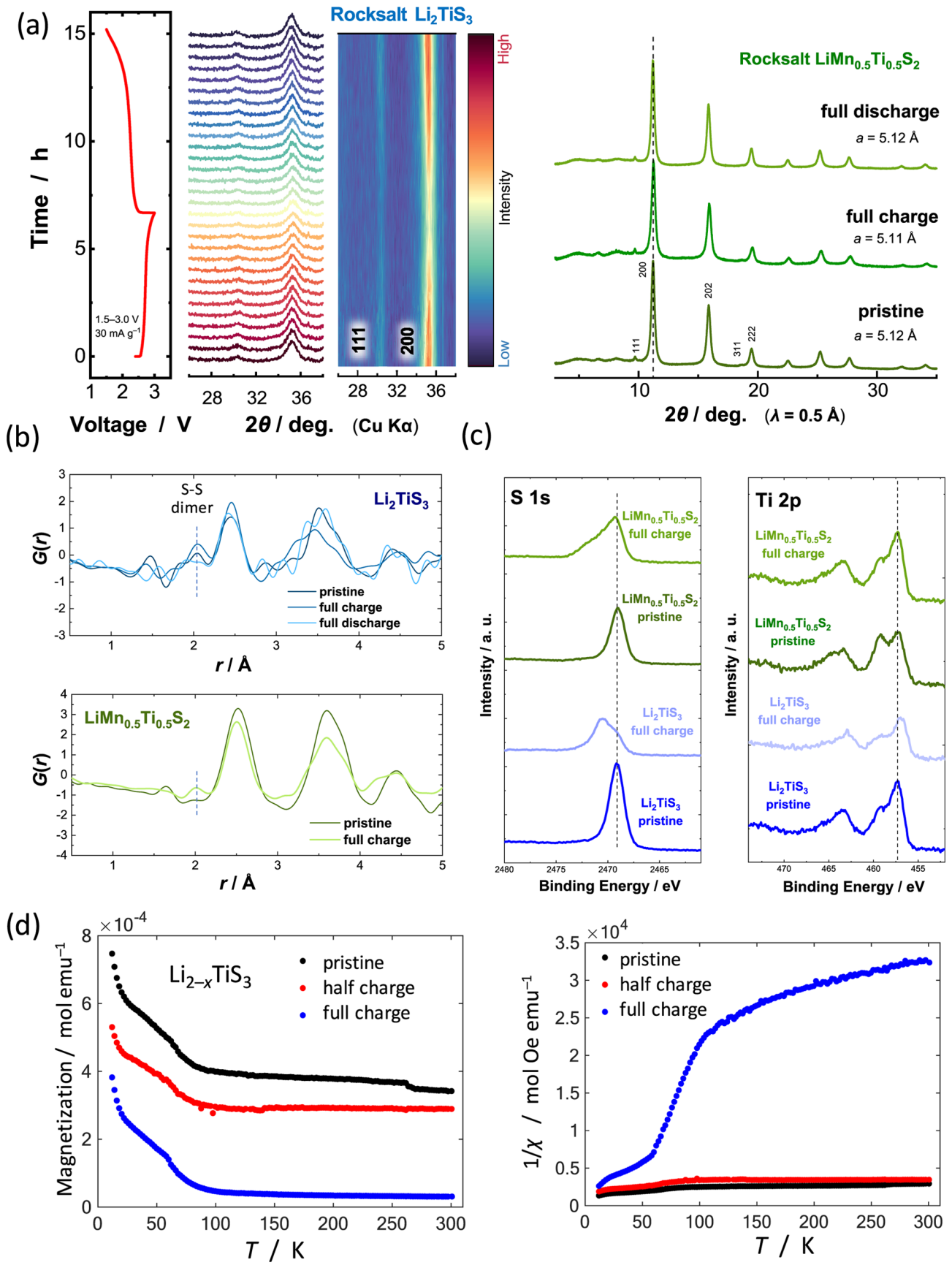

Figure 3. Reaction mechanisms of disordered (rocksalt) $Li_{2-x}TiS_3$ and $Li_{1-x}Mn_{0.5}Ti_{0.5}S_2$: (a) *In situ* XRD data of Li_2TiS_3 and *ex situ* synchrotron XRD data of $LiMn_{0.5}Ti_{0.5}S_2$ during charge/discharge. Comparison of (b) pair distribution functions and (c) HAXPES spectra for both samples. (d) Results of magnetic measurements for disordered (rocksalt) $Li_{2-x}TiS_3$.

https://doi.org/10.1021/jacs.5c04018
J. Am. Chem. Soc. 2025, 147, 26238−26253

compared with total X-ray scattering with pair distribution function (PDF) analysis as shown in Figure 1c. A clear difference in the first coordination shells for both samples is noted. Lower peak intensity is observed for rocksalt Li_2TiS_3, which is indicative of a local distortion for the nanosized sulfide with enriched grain boundaries. In addition, a peak intensity difference is more clearly visible as the r value increases, indicating that long-range ordering is more significant for the layered phase as expected from the difference in crystallinity for both samples. These differences in local structures are further evidenced from ^{7}Li magic angle spinning nuclear magnetic resonance (MAS NMR) spectroscopy. ^{7}Li MAS NMR spectra of both samples with different spinning speeds (0−20 kHz) are shown in Figure 1d. Peak width of NMR spectra is broader for rocksalt Li_2TiS_3, which is indicative of a diverse local environment for Li ions associated with cation disordering. These findings are consistent with each other; nanosized and disordered phases are formed by mechanical milling, and highly crystalline phase with a higher local symmetry is formed by subsequent heating process.

Electrochemistry of Li_2TiS_3 and $LiMn_{0.5}Ti_{0.5}S_2$ Polymorphs. Electrochemical properties of rocksalt and layered Li_2TiS_3 are compared, and galvanostatic charge/discharge curves of both samples are shown in Figure 2a. Layered Li_2TiS_3 is electrochemically inactive, whereas rocksalt Li_2TiS_3 shows superior electrode reversibility. Note that the layered sample shows a very small reversible capacity even after being charged to 4.5 V in Li cells. In contrast, layered $LiMn_{0.5}Ti_{0.5}S_2$, which has been synthesized with the same methodology with layered Li_2TiS_3, is electrochemically active and shows a reversible capacity of 125 mA h g^{-1}, corresponding to approximately 60% of the theoretical capacity based on Li contents in the host structure and one electron redox ($LiMn_{0.5}Ti_{0.5}S_2 \rightarrow \square Mn_{0.5}Ti_{0.5}S_2 + Li^+ + e^-$, herein "□" denotes a vacant octahedral site). Moreover, similar to Li_2TiS_3, disordered $LiMn_{0.5}Ti_{0.5}S_2$ shows a better electrode performance compared with that of the layered sulfide. This difference originates from superior electronic conductivity for the rocksalt structure, as shown in Supporting Figure S2. A methodology of conductivity measurements for powder samples is found in the literature.[26] Nearly 10 times higher electronic conductivity is observed for Li_2TiS_3 with the rocksalt structure. The resistivity of the samples was calculated to be 160 Ω·m for rocksalt Li_2TiS_3 and 1600 Ω·m for the layered Li_2TiS_3. It should be noted that the resistivity was measured using compressed powder pellets (area: 0.79 cm^2, thickness: 1 mm) without sintering. The resistivity values obtained from compressed powder samples are expected to be higher than those of sintered samples due to grain boundary resistance and the presence of pores. The enrichment of structural defects with a higher concentration of grain boundary induced by high-energy mechanical milling may increase electronic conductivity. A similar phenomenon, the improvement of electronic conductivity for nanosized disordered oxides synthesized by mechanical milling, has also been reported.[26] Electron delocalization, coupled with band broadening, is also expected because more complicated local structures are formed for materials with the cation-disordered rocksalt structure,[14,16] as evidenced by NMR study (Figure 1d). In addition, ionic conductivity is influenced by the local structures of grain boundaries,[27] and therefore, the structural defects affect ionic conductivity for these nanosized sulfides. Activation of anionic redox for Li_2TiS_3 with ordered and disordered structures is further discussed in the theoretical section.

Initial charge capacities for both rocksalt sulfides are slightly smaller compared with the second cycle, which originates from partial oxidation of the samples. Similar phenomena are known for the samples with high surface area synthesized by high-energy mechanical milling.[26,28] Such oxidation reaction during mechanical milling is mediated for the samples with lower electrode potential, <3 V vs. Li/Li$^+$, presumably associated with oxidation by water and other protonated solvents coupled with hydrogen molecule generation. Although a large reversible capacity of 350 mA h g^{-1} (Figure 2a), which nearly corresponds to the theoretical capacity of Li_2TiS_3, is obtained for the sample with the rocksalt structure, its reversibility is rapidly lost on electrochemical cycles (Figure 2b). The capacity fading originates from the dissolution of sulfide ions into electrolyte solutions with polar solvents, and therefore, its reversibility of lithium-containing metal sulfides as electrode materials is significantly improved by using a polymer-based solid electrolyte.[15] Similarly, the use of highly concentrated electrolyte solutions is also known to be beneficial to mitigate the dissolution of soluble species, like V and Mn ions because of the absence of free solvent molecules.[28,29] Therefore, 7.25 mol kg^{-1} $LiBF_4$ dissolved in propylene carbonate (PC)[30] was used as an electrolyte solution. Although 7.25 mol kg^{-1} $LiBF_4$/PC shows lower ionic conductivity (0.141 mS cm^{-1}) because of high viscosity,[30] much improved reversibility as electrode materials is obtained for the rocksalt Li_2TiS_3 cycled with the concentrated electrolyte (Figure 2c). Good capacity retention, no capacity fading for continuous 40 cycles, is achieved, as shown in Figure 2d.

It is anticipated that Li_2TiS_3 ($Li_{1.33}Ti_{0.67}S_2$) shows inferior electronic conductivity compared with $LiMn_{0.5}Ti_{0.5}S_2$ because Li_2S is an insulator and the enrichment of Li ions in the host structure results in lowered electronic conductivity. Nevertheless, much better rate capability as electrode materials is observed for Li_2TiS_3 with the rocksalt structure (Figure 2e). Li_2TiS_3 delivers a discharge capacity of >250 mA h g^{-1} even at a rate of 1920 mA g^{-1}. In contrast, a discharge capacity of <100 mA h g^{-1} at the same rate is observed for $LiMn_{0.5}Ti_{0.5}S_2$. This fact indicates that discharge rate capability for both materials is limited by the percolative Li-ion conduction,[31] and not by the electronic conduction. The enrichment of Li ions in the host structure results in improved percolative conduction of Li ions, leading to superior ionic conductivity and rate capability as electrode materials.

Reaction Mechanisms of Li_2TiS_3 and $LiMn_{0.5}Ti_{0.5}S_2$ with the Rocksalt Structure. To study the reaction mechanism of two different sulfides with the rocksalt structure, Li_2TiS_3 and $LiMn_{0.5}Ti_{0.5}S_2$, an XRD study was used for electrochemically charged/discharged samples. As shown in Figure 3a, for $Li_{2-x}TiS_3$, a clear reduction in crystallinity is noted after charge to 3.0 V and full extraction of Li ions (also see Supporting Figure S3), suggesting that an amorphous phase is partially formed after oxidation in a Li cell. A similar observation was also reported in the literature.[11] In contrast, higher crystallinity is retained for $Li_{1-x}Mn_{0.5}Ti_{0.5}S_2$, and the formation of the amorphous phase is relatively mitigated for the non-Li-excess and stoichiometric metal sulfide. However, both materials show higher crystallinity after full discharge (rereduction) to 1.5 V in a Li cell, suggesting that the amorphous phase formed on charge is recrystallized on discharge as a reversible process.

https://doi.org/10.1021/jacs.5c04018
J. Am. Chem. Soc. 2025, 147, 26238−26253

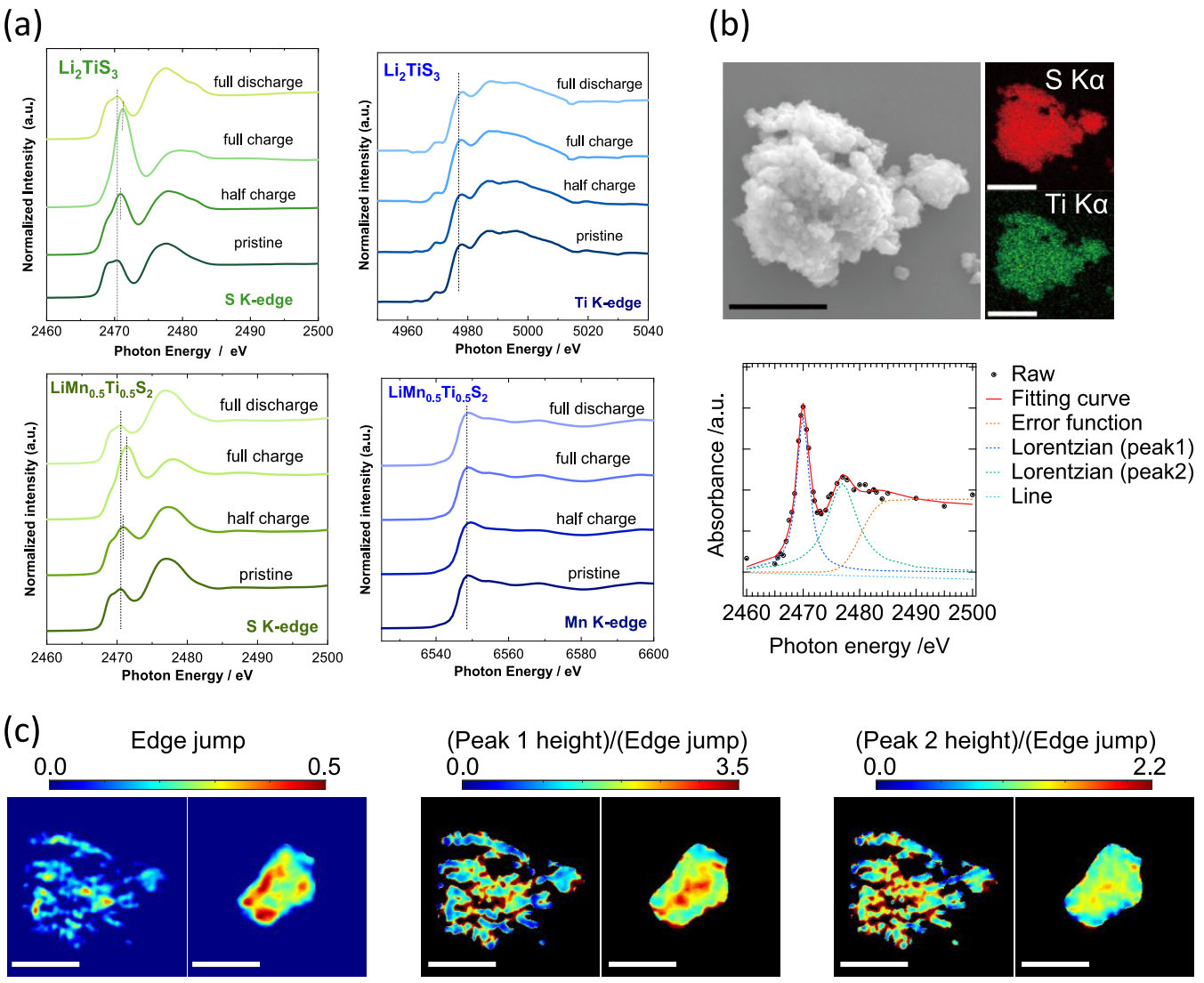

Figure 4. Study of changes in electronic structures by XAS spectroscopy: (a) Comparison of XAS spectra for disordered (rocksalt) $Li_{2-x}TiS_3$ and $Li_{1-x}Mn_{0.5}Ti_{0.5}S_2$, (b) SEM/EDX spectra of half-charged $Li_{2-x}TiS_3$ with the disordered structure and an example of curve fitting for a reconstructed absorption spectrum of full-charged $Li_{2-x}TiS_3$, (c) chemical state maps of edge-jumps and normalized peak heights of (left) half-charged and (right) fully charged samples obtained by X-ray spectroscopic ptychography measurements. Scale bars correspond to 2.5 μm.

A local structure study by PDF analysis further reveals that the amorphous phase formation observed on charge clearly correlates with a S−S dimer formation, as shown in Figure 3b. The largest peak at 2.5 Å can be assigned to a chemical bond between Ti and S in Li_2TiS_3. The peak intensity at 2.05 Å is intensified after charge, which can be assigned as the formation of S−S dimers.[11] This peak is also observed for the pristine sample of Li_2TiS_3 because partial oxidation during material synthesis is unavoidable as mentioned above (Figure 2a). However, after the discharge process to 1.5 V, the peak originating from the S−S dimers is clearly less intensified. Note that a similar peak at 2.05 Å also appears for $Li_{1-x}Mn_{0.5}Ti_{0.5}S_2$ after charge to 3.0 V, but the more intensified peak is observed for $Li_{2-x}TiS_3$, which is consistent with the fact that the non-negligible fraction of the amorphous phase is formed for $Li_{2-x}TiS_3$ compared with $Li_{1-x}Mn_{0.5}Ti_{0.5}S_2$ (Figure 3a).

Charge compensation by the solid-state redox reaction of sulfide ions was further examined by hard X-ray photoelectron spectroscopy (HAXPES). Compared with soft X-ray PES, information from relatively thicker regions (~10 nm from the surface) can be obtained by HAXPES because of the higher kinetic energy for ejected electrons (photoelectrons). For S 1s HAXPES spectra of the pristine samples, a clear peak centered at 2469 eV is observed for both samples (Figure 3c), which can be assigned as a sulfide ion, S^{2-}. After charge, a new peak appears at a higher binding energy region, ~2471 eV, and the intensity of the original peak for sulfide ions at 2469 eV is clearly weakened associated with oxidation of sulfide ions followed by partial dimerization of sulfur species. The original peak of sulfide ions is clearly enriched for $Li_{1-x}Mn_{0.5}Ti_{0.5}S_2$ after charge to 3.0 V, which is consistent with the results of XRD and PDF analysis, *i.e.*, the partial mitigation of S−S dimerization for $Li_{1-x}Mn_{0.5}Ti_{0.5}S_2$. In contrast to S 1s HAXPES spectra, no clear change is found in Ti 2p HAXPES spectra (Figure 3c), indicating that Ti ions are not responsible for the charge compensation as expected from the nature of Ti^{4+} ions with d^0 configuration.

To identify redox species in $Li_{2-x}TiS_3$, the magnetic susceptibility (χ) is measured before and after charge.[32] For $Na_{2-x}Mn_2O_7$, the hole formation and stabilization in anionic

https://doi.org/10.1021/jacs.5c04018
J. Am. Chem. Soc. 2025, 147, 26238−26253

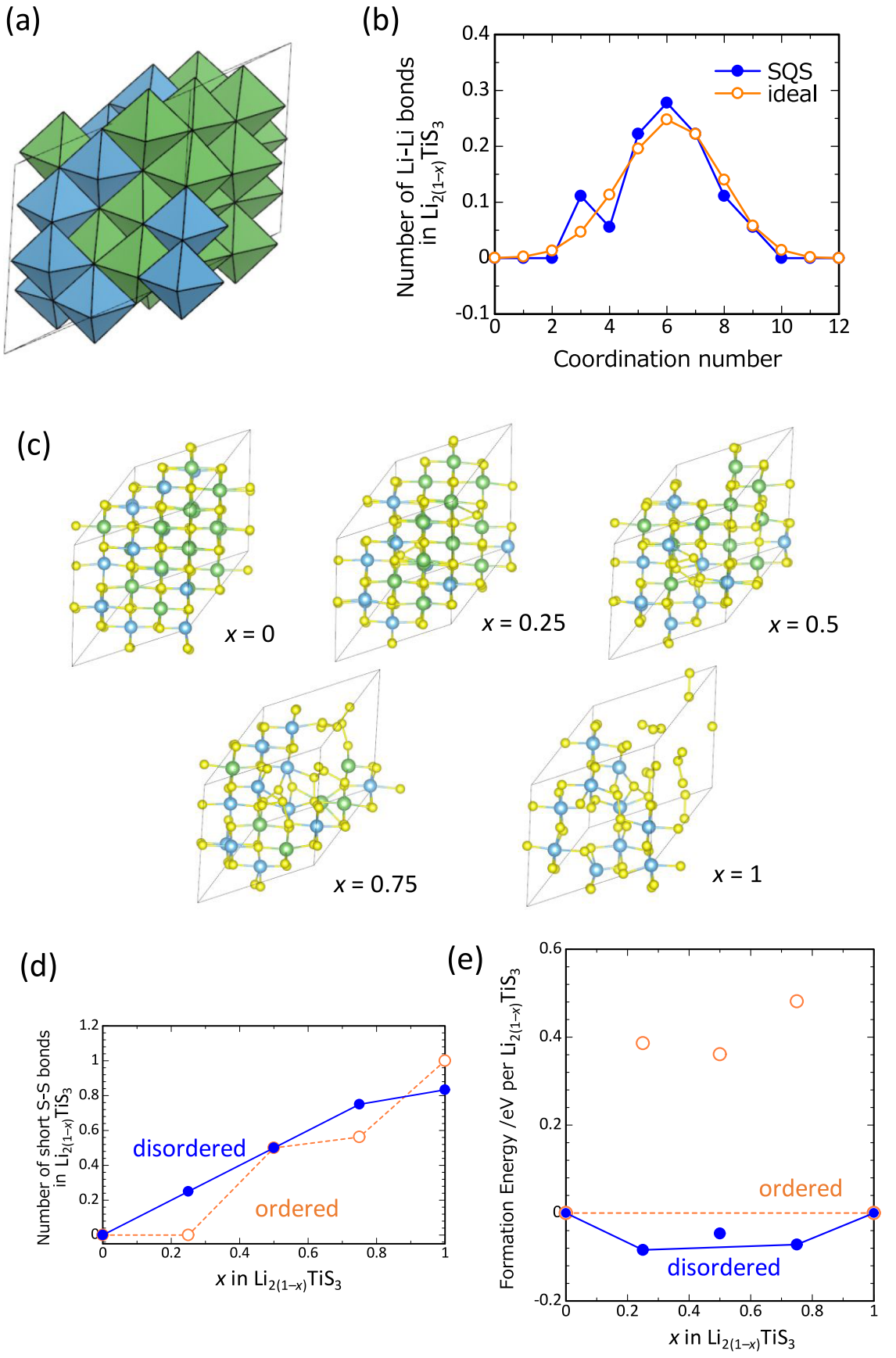

Figure 5. (a) Crystal structure of disordered rocksalt Li_2TiS_3 derived from special quasi-random structure (SQS) approach. The simulation cell composition is $Li_{24}Ti_{12}S_{36}$. (b) Coordination number distribution between Li and nearest neighbor Li ions (Li−Li bonds). Blue and orange lines correspond to SQS-derived simulation cell (panel (a)) and ideal random structure which considers random Li/Ti arrangement using large cell consisting of 1 000 000 cation sites. Coordination number distribution for Li−Ti and Ti−Ti interactions are also considered for simulation cell

https://doi.org/10.1021/jacs.5c04018
J. Am. Chem. Soc. 2025, 147, 26238−26253

Figure 5. continued

building derived from SQS approach. (c) Evolution of crystal structure with delithiation process from disordered sample cell, i.e., $Li_{24(1-x)}Ti_{12}S_{36}$ (x = 0, 0.25, 0.5, 0.75, and 1.0), where Li/vacancy arrangement for intermediate compositions in the structure inputs are derived from genetic algorithm (GA) approach. Yellow, light-blue, and green spheres indicate sulfur, titanium, and lithium atoms, respectively. (d) Number of short S−S bonds (bond length of S−S is less than 2.2 Å) as a function of composition x in $Li_{2(1-x)}TiS_3$ (x = 0, 0.25, 0.5, 0.75, and 1.0). Blue and orange lines represent delithiation process from disordered and ordered structures, respectively. (e) DFT calculated formation energies as a function of composition x in $Li_{2(1-x)}TiS_3$. Blue and orange symbols represent DRS and LRS structures, respectively. Tie lines correspond to convex hull.

species were efficiently detected by the magnetic measurement.[33] A similar methodology can be applied for $Li_{2-x}TiS_3$ as shown in Figure 3d. For the fully charged sample to 3.0 V, a slope of $1/\chi$ as a function of temperature below 50 K and above 100 K is clearly large compared with the pristine and half-charged samples, indicating that a value of the Curie constant is the smallest among the three samples. When the holes are electrochemically formed and stabilized in sulfide ions, an increase in values of Curie constant is anticipated because of the absence of magnetic active species in pristine sample.[33] This finding indicates that holes cannot be stabilized in $Li_{2-x}TiS_3$, and S−S dimerization is the dominant process upon charge in Li cells. A nonlinear change in $1/\chi$ between 50 and 100 K suggests a phase transition at this temperature range, which is out of scope for this article.

X-ray Absorption Study on Disordered $Li_{2-x}TiS_3$ and $Li_{1-x}Mn_{0.5}Ti_{0.5}S_2$. To further elucidate the charge compensation process by the solid-state redox reaction of sulfide ions, X-ray absorption (XAS) spectroscopy was adopted. S K-edge and Ti K-edge XAS spectra collected with a fluorescence yield mode for $Li_{2-x}TiS_3$ and $Li_{1-x}Mn_{0.5}Ti_{0.5}S_2$ are shown in Figure 4a. Two major peaks, a pre-edge peak centered at 2470 eV and a broad peak at 2477 eV, are observed, and a similar XAS profile is observed for Li_2S.[34] A clear peak shift to a higher energy region is observed for pre-edge spectra at the S K-edge of $Li_{2-x}TiS_3$ on charge, which is indicative of sulfur oxidation, and this result is consistent with the observation of HAXPES (Figure 3c). Peak top energy is shifted by 1 eV coupled to peak sharpening after full charging for $Li_{2-x}TiS_3$. Moreover, no change is observed for Ti K-edge XAS spectra after discharge, indicating that Ti ions cannot be electrochemically reduced on discharge. These observations conclude that only sulfide ions are responsible for charge compensation without the contribution of Ti ions as redox species. For $Li_{1-x}Mn_{0.5}Ti_{0.5}S_2$, a similar observation is noted for S K-edge spectra. Moreover, the oxidation of Mn^{2+} ions is not evidenced after the charge to 3.0 V in Li cells. Similarly, for $Li_{1-x}Fe_{0.5}Ti_{0.5}S_2$, the oxidation of Fe^{2+} ions is not evidenced as reported in the literature.[15] When the peak profiles of fully charged samples for $Li_{2-x}TiS_3$ and $Li_{1-x}Mn_{0.5}Ti_{0.5}S_2$ are compared, a larger pre-edge peak at 2471 eV is observed for $Li_{2-x}TiS_3$, which is consistent with the experimentally observed larger charge capacity and thus more pronounced oxidation of S species in $Li_{2-x}TiS_3$ (Figure 2). These results suggest that sulfide ions are mainly responsible for charge compensation without the contribution of transition metal ions with d electrons. This finding is also supported by the fact that similar operation voltage, ∼2.5 V, is observed for both $Li_{2-x}TiS_3$ and $Li_{1-x}Mn_{0.5}Ti_{0.5}S_2$ ($Li_{1-x}Fe_{0.5}Ti_{0.5}S_2$[15]) as shown in Figure 2a, regardless of the presence of other transition metal ions with d electrons. The d electron bands for Mn and Fe ions for sulfide-based materials are found at a lower energy region compared with sulfur 3p bands, leading to a unique nature as electrode materials, which cannot be observed for conventional layered oxides with transition metal ions such as $LiCoO_2$ and $LiNiO_2$. Therefore, band broadening for sulfide-based materials with the disordered structure, presumably coupled with the formation of defect bands near Fermi level for nanosized crystalline samples, leads to improved electronic conductivity.

To further validate the electronic and chemical natures of $Li_{2-x}TiS_3$ with a high spatial resolution (∼100 nm), X-ray spectroscopic ptychography measurements were conducted at the S K-edge. Half-charged and fully charged samples were obtained by chemical oxidation. To confirm distributions of S and Ti ions in the oxidized particles, prior to the ptychography study, SEM/EDX spectroscopy was applied (Figure 4b and S4a), and the results indicate that S and Ti ions are uniformly found in the particles without segregation. The detailed methodology for ptychography analysis is described in our publication.[35,36] Reconstructed absorption and reconstructed phase images are shown in Supporting Figure S4b with 20 nm pixel size resolution. The particle shapes in the phase images, which contain information on electron amounts, for both samples are similar to those of SEM images. From the reconstructed absorption and phase images, spatially resolved S K-edge XAS and phase spectra are also obtained in Supporting Figure S4c. The spatially resolved XAS spectra show similar profiles to those of the conventional spectra (Figure 4a). Chemical state mapping was obtained by the curve-fitting analysis of spatially resolved XAS spectra and the phase images. An example of a curve-fitting analysis is shown in Figure 4b. Two major peaks, peaks 1 and 2, were fitted, and chemical state mapping was obtained by the normalization of peak intensities by edge jump, as shown in Figures 4c and S5. The average energy of peak 2 position is increased for the fully charged sample compared with the half-charged sample (Supporting Figure S5), indicating that average oxidation states of sulfide ions are increased for the fully charged sample. Moreover, nonuniformity for the chemical oxidation states for sulfur species is noted for both samples, suggesting that different local structures for sulfide ions are formed for the charged samples. Such nonuniformity of electrochemical reactions for the compounds with the disordered structure is further discussed in the theoretical section.

Theoretical Analysis of Delithiation from Li_2TiS_3 with Ordered and Disordered Structures. For theoretical study, two types of structures, ordered layered and disordered rocksalt structures, are considered for Li_2TiS_3. The Li/Ti configuration for layered Li_2TiS_3 structure was referred to that of layered Li_2TiO_3.[37] On the other hand, special quasi-random structure (SQS) approach[38] was performed to mimic random configuration for Li_2TiS_3 cell consisting of a relatively small number of atoms. In this study, only two-body interactions are considered between adjacent cation−cation pairs (Li−Li, Li−Ti, and Ti−Ti), and candidate structures are generated by the Metropolis Monte Carlo simulation. Figure 5a displays the obtained SQS-derived cell, $Li_{24}Ti_{12}S_{36}$, and distribution of coordination numbers (CNs) of the nearest neighbor Li−Li

https://doi.org/10.1021/jacs.5c04018
J. Am. Chem. Soc. 2025, 147, 26238−26253

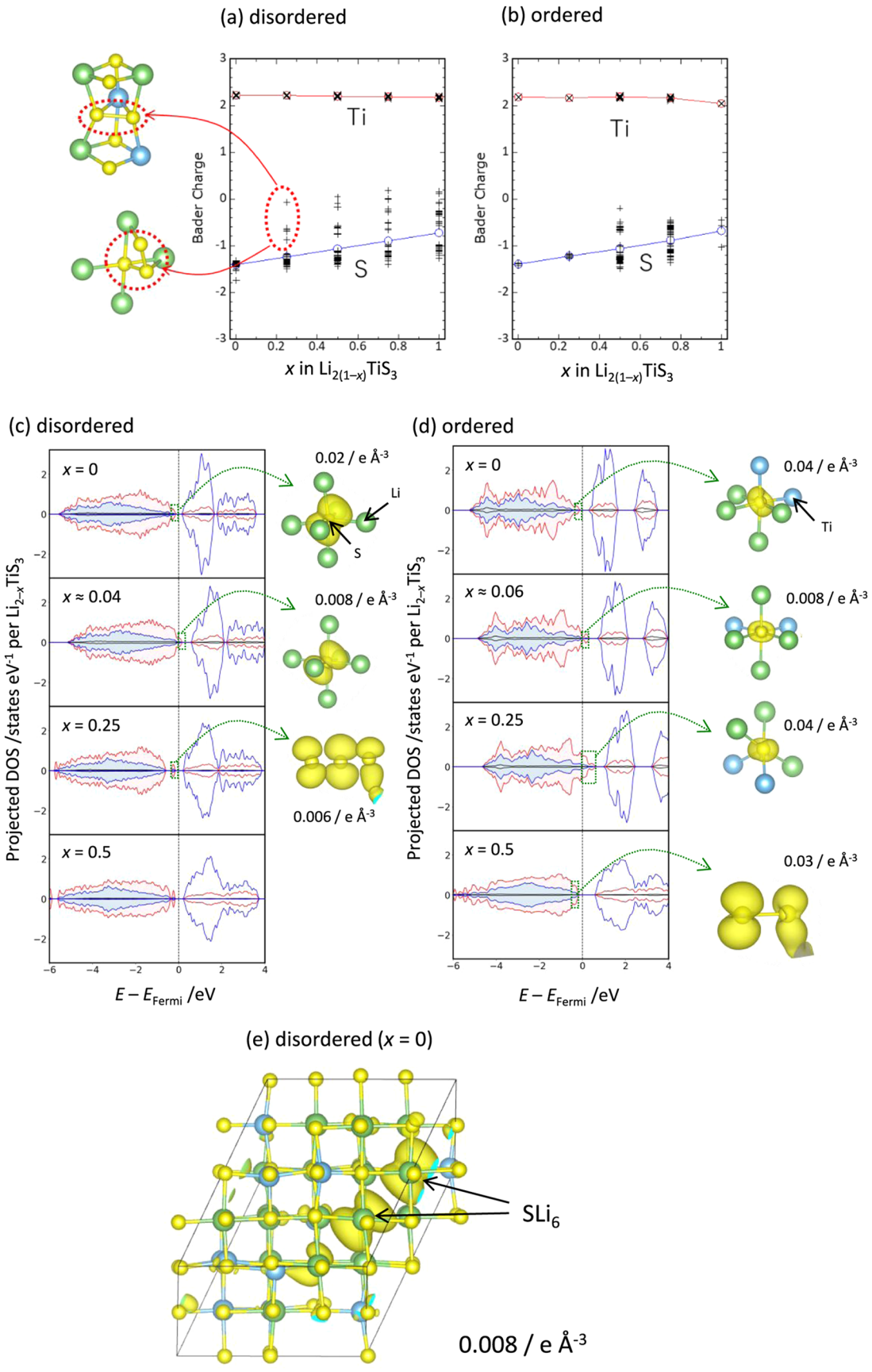

Figure 6. (a) Bader charges for Ti and S ions as a function of composition x in (a) disordered and (b) ordered $Li_{2(1-x)}TiS_3$. Cross symbols refer to an individual Ti or S ion, while lines correspond to averaged Bader charges for Ti or S ions. Projected density of states (PDOS) for Ti and S in (c) disordered and (d) ordered $Li_{2(1-x)}TiS_3$ (x = 0, 0.25, and 0.5). Blue and red lines correspond to PDOS for Ti and S, respectively. (c−e) Partial

https://doi.org/10.1021/jacs.5c04018
J. Am. Chem. Soc. 2025, 147, 26238−26253

Figure 6. continued

electron/hole densities around Fermi level (marked as hatched line) are visualized as isosurface projections at the side of PDOS diagrams at different isovalues. Yellow, light-blue, and green spheres correspond to S, Ti, and Li atoms, respectively.

interactions as an example (Figure 5b). A good accordance of the CN distribution is indicated between SQS structure and ideal random structure. The energy of ordered Li_2TiS_3 is 0.334 eV per Li_2TiS_3 unit lower (more stable) than that of disordered Li_2TiS_3, which corresponds to the order−disorder phase transition temperature at approximately 2030 K by solely considering the configurational entropy effect arising from Li/Ti arrangements. According to Lun et al.,[39] the temperature of 2573 K corresponds to the high-energy conditions generated with ball milling in Li−Mn−O−F chemical species. This result is also consistent with the fact that the disordered phase synthesized by high-energy milling is a metastable phase and changes into the ordered phase by heating (Figure 1a). However, the difference between the estimated phase transition temperature derived from the configurational entropy and the actual ball-milling synthesis temperature is relatively small. As a result, uniform formation of the disordered phase may not be fully achieved during the synthesis, potentially leading to a certain degree of compositional inhomogeneity. The experimentally observed nonuniform features at the particle scale in the ptychography results are thus likely to reflect the inhomogeneous distribution of the disordered phase characterized by SLi_6 coordination environments. Because the electrochemical Li extraction is performed around room temperature, the SQS approach that assumes high-temperature extreme configuration is not appropriate to determine Li/vacancy arrangement of delithiated $Li_{2-x}TiS_3$ phase. Instead, the genetic algorithm (GA) approach is used to optimize the Li/vacancy configuration in the fixed ordered and disordered $\square_2TiS_3$ flameworks ($\square$ denotes vacant sites). The superstructures of $Li_{32(1-x)}Ti_{16}S_{48}$ and $Li_{24(1-x)}Ti_{12}S_{36}$ are used for ordered and disordered flameworks,[40−43] respectively. Details on the GA optimization are described elsewhere.[40−43]

Figure 5c shows GA optimized disordered $Li_{2(1-x)}TiS_3$ (x = 0, 0.25, 0.5, 0.75, and 1), and Figure 5d summarizes variation of the number of S−S bonds whose length is less than 2.1 Å as a function of composition x for both ordered and disordered structures. As the delithiation proceeds, the number of short S−S bond formations, i.e., formation of disulfide (S_2^{2-}), increases. Hence, the disulfide formation by the oxidation reaction of sulfide ions, such as $2S^{2-} \rightarrow S_2^{2-} + 2\ e^-$, is mediated during electrochemical Li removal. Note that trisulfide (S_3^{2-}) and tetrasulfide (S_4^{2-}) ions are also found, as shown in Figure 5c. Short S−S bonds are not formed for the composition x = 0.25 with ordered structure, indicating another oxidation reaction mechanism as discussed later.

Phase stability of partially delithiated compositions was further evaluated by plotting formation energies, ΔE_f, as displayed in Figure 5e. The formation energy is computed using total electron energies of the end compositions (x = 0 and 1) as references.

$$\Delta E_f\ (Li_{2(1-x)}\ TiS_3) = E_0\ (Li_{2(1-x)}\ TiS_3) - (1-x)\ E_0\ (Li_2TiS_3) - x\ E_0\ (TiS_3) \quad (1)$$

where E_0 (X) corresponds to the total electron energy of composition X. Formation energies of intermediate compositions in ordered $Li_{2(1-x)}TiS_3$ are positive, indicating two-phase coexistence reaction between fully lithiated (x = 0) and delithiated (x = 1) compositions. On the other hand, formation energies are slightly negative for the partially delithiated phase of disordered $Li_{2(1-x)}TiS_3$, suggesting that the reaction is likely to proceed in a solid-solution manner. This result is also consistent with the finding by an experimental study in Figure 3a. The calculated voltage profiles are shown in Supporting Figure S6. The onset voltage of delithiation for both ordered and disordered Li_2TiS_3 is calculated to be ∼2.2 V. Gradual increase of voltage up to ∼2.5 V is visible for disordered Li_2TiS_3 because of solid-solution reaction, while the voltage for ordered Li_2TiS_3 is constant due to the two-phase coexistence reaction. The calculated voltage for the delithiation from ordered Li_2TiS_3 via metastable solid solution route is ∼3 V, which is more than ∼0.8 V higher than that of the equilibrium two-phase coexistence reaction. However, the fact is that ordered Li_2TiS_3 is electrochemically inactive, ∼4.5 V in Li cells (Figure 2a), suggesting that anionic redox of the ordered phase is hindered by a kinetic limitation as discussed in the next section.

Nonuniform Li Extraction for $Li_{2-x}TiS_3$ with the Cation-Disordered Structure. Bader charge analysis was performed for disordered and ordered $Li_{2-x}TiS_3$ to elucidate oxidation reaction mechanisms including metastable delithiated phases (Figure 6a,b). In both phases, Bader charges of Ti ions are almost constant regardless of composition x, indicating that no electron exchange reaction occurs at Ti ions, keeping the Ti^{4+} (d^0) electronic configuration during delithiation. On the other hand, a gradual increase in averaged Bader charges of sulfide ions is observed, indicating oxidation of sulfur species during delithiation. In detail, Bader charges of S ions are almost the same as ca. −1.2 at composition x = 0 (before delithiation), suggesting little local structure configuration effect in the disordered phase. Bader charges for several S atoms in disordered $\square_{0.5}Li_{1.5}TiS_3$ (x = 0.25) show discontinuous increases ranging from −1.0 to 0, which is attributed to the formation of disulfide ions (S_2^{2-}) and trisulfide ions (S_3^{2-}) as shown in Figure 6c. On the other hand, Bader charges for all the S ions show a slight increase in metastable ordered $\square_{0.5}Li_{1.5}TiS_3$ (x = 0.25) as shown in Figure 6b, which corresponds to the no short S−S bond formation. In both disordered and ordered structures, an electronic exchange for the oxidation reaction proceeds by the formation of disulfide, trisulfide, and tetrasulfide ions at composition $x \geq 0.5$.

Projected density of states for Ti and S atoms and visualized electron (hole) densities near the Fermi level for disordered and ordered $Li_{2(1-x)}TiS_3$ (x = 0, 0.25, and 0.5) are also shown in Figure 6c,d. In both structures, valence and conduction bands are composed of mainly S 3p and partially Ti 3d orbitals, respectively. Bandgaps for disordered and ordered Li_2TiS_3 are 0.65 and 0.79 eV, respectively, by evaluating the difference in the total energies between the system containing electron, hole, and neutral cell.[44,45] Such band gap broadening is expected to originate from diverse local structures for

https://doi.org/10.1021/jacs.5c04018
J. Am. Chem. Soc. 2025, 147, 26238−26253

disordered Li_2TiS_3. A similar discussion was provided for ordered and disordered Li_3NbS_4[14] and vanadium-based oxides.[16] Furthermore, the presence of a unique local environment for sulfide ions in the disordered phase, which cannot be formed for ordered Li_2TiS_3, is noted. The valence band maximum (VBM), where electron extraction occurs by electrochemical delithiation, is visualized as partial electron densities for both disordered and ordered Li_2TiS_3 at composition $x = 0$. The visualized electron density corresponding to VBM of disordered Li_2TiS_3 is localized for the specific two sulfide ions as shown in Figure 6e (also see Figure 6c, $x = 0$), and both sulfide ions are surrounded by 6 Li ions. This is due to a nonbonding nature between Li and sulfide ions, while partially covalent bonding formation between Ti and sulfide ions reduces the energy level of the occupied orbital states. This unique local environment for sulfide ions, SLi_6, is formed only for the disordered phase. The electrons (or holes) in the orbitals near the VBM appearing in the SLi_6 environment seem to be localized based on the figure. Therefore, the orbital density at each energy level projected onto the radius of the augmentation sphere used in the projector-augmented wave (PAW) method was evaluated as a measure of localization (Supporting Figure S7a,b). A localization value close to 1 indicates strong localization, whereas a smaller value suggests delocalization. The results showed that the localization value near the valence band (S 3p orbital) is approximately 0.6 for both disordered and ordered Li_2TiS_3, with no significant difference observed. In contrast, for the corresponding oxide model of disorder Li_2TiO_3 based on the disordered Li_2TiS_3, crystal structure, the localization value increased to 0.8 (Supporting Figure S7c). Considering that the PAW sphere radius for oxygen is smaller than that for sulfur, the electrons in the oxide are considered to be more localized around the O atoms at the OLi_6 configuration. In addition, upon slight Li extraction from Li_2TiS_3 (in Figure 6c, disordered, and in Figure 6d, ordered models), the compositions correspond to approximately $x \sim 0.04$ and $x = 0.06$, respectively (hereafter, such slightly delithiated compounds are referred to as $Li_{2-\delta}TiS_3$), the PDOS reveals that hole states appear near the Fermi level ($E - E_F < 0.3$ eV) in both disordered and ordered models. These hole states match the orbitals near the VBM prior to delithiation and originate from the S 3p orbitals (Figures 6c,d and S8). When delithiation starts in disordered Li_2TiS_3 by electrochemical oxidation, Li ions are nonuniformly extracted from SLi_6 environment, and such nonuniformity for Li extraction is also consistent with the experimental finding by ptychography study (Figure 4c). On the other hand, all the sulfide ions are surrounded by 4 Li and 2 Ti ions in ordered Li_2TiS_3. Partial electron density for VBM of ordered Li_2TiS_3 ($x = 0$) shown in Figure 6d indicates an S 3p-derived orbital. As reported, 180° Li−O−Li configuration is the primary reason for electrochemically active O 2p orbital formation due to nonbonding interaction, and this nonbonding (localized) O 2p orbital forms along the Li−O−Li direction.[46,47] However, the visualized partial electron density around VBM does not show dumbbell- or ellipse-shaped nonbonding S 3p orbital along the Li−S−Li axis (Figure 6d). Therefore, unlike oxides, in sulfides, the S 3p orbitals do not appear to be localized even when Li−S−Li configurations are formed. This is also supported by the lower localization factor observed in sulfides compared to oxides (Supporting Figure S7). Furthermore, in the disordered $Li_{2-\delta}TiO_3$ oxide, hole states formed upon slight delithiation appear approximately 0.4 eV above the Fermi level and are observed exclusively in the down-spin channel (Supporting Figure S8). This spin asymmetry suggests the presence of strong electron−electron Coulomb interactions within the partially occupied orbitals. Such spin-polarized localization of holes is characteristic of systems with strong electronic correlations, where intraorbital Coulomb repulsion leads to spin splitting and preferential occupancy of a single-spin channel. This behavior is commonly captured in correlated-electron models such as the Hubbard model and reflects the Mott-like nature of the hole states.[48,49] Therefore, polaronic electron conduction is likely to proceed in disordered $Li_{2-x}TiO_3$ oxide electrode as reported in various oxide electrodes.[50−52] In contrast, in the corresponding disordered sulfide $Li_{2-\delta}TiS_3$, there was no significant difference in the DOS between spin-up and spin-down states, and the band structure was metallic-like (in fact, one of the bands was found to cross the Fermi level). These observations imply that electron correlation effects are weak and that electrical conductivity in the sulfide is governed by band conduction. Note that the absolute values of the spin moments, which are defined as the difference between spin-up and spin-down components within the augmentation spheres of each atom, were found to be less than 0.0001 μ_B throughout the composition range $0 \leq x \leq 0.5$ in the DFT calculations performed for $Li_{2-x}TiS_3$. This result is consistent with the nearly identical shapes of the spin-up and spin-down PDOS shown in Figure 6c. Furthermore, the magnetic susceptibility measurements shown in Figure 3d exhibit paramagnetic behavior down to near absolute zero, in good agreement with the nonmagnetic nature suggested by the present DFT results. A similar trend was also observed in layered-type and ordered $Li_{2-\delta}TiS_3$. However, the hole states tended to separate from the valence band. This indicates that initial delithiation in disordered Li_2TiS_3 results in the formation of metallic-like bands and relatively high electronic conductivity, whereas ordered Li_2TiS_3 exhibits a tendency to open a gap at the Fermi level, leading to lower electronic conductivity. Taken together, these findings are consistent with the electrochemical inactivity of ordered Li_2TiS_3 (Figure 2a) and the experimental results shown in Supporting Figure S2.

The difference in structures, disordered and ordered phases, and (non)uniformity of delithiation for both phases also change dimerization processes for sulfide ions on oxidation. At the composition $x = 0.25$, a localized band (occupied) is formed in disordered $\square_{0.5}Li_{1.5}TiS_3$, and the visualized partial electron density indicates that the localized band is attributed to the trisulfide ion, S_3^{2-} (Figure 6c, also see Figure 5c). Meanwhile, a metallic-like band is formed due to electron extraction (hole creation) from the S 3p band in ordered $\square_{0.5}Li_{1.5}TiS_3$ ($x = 0.25$) as follows the rigid-band model (Figure 6d). This theoretical finding indicates no formation of short S−S bonds for ordered $\square_{0.5}Li_{1.5}TiS_3$. The existence or absence of short S−S bonds in both phases is owed to vacancy configurations and structural distortions after delithiation. Li vacancies are selectively formed and enriched around the S ions coordinated with 6 Li ions in disordered $\square_{0.5}Li_{1.5}TiS_3$, and the enriched vacant sites allow to cause structural distortions to form S−S bonding. In the computational model of disordered $\square_{0.5}Li_{1.5}TiS_3$ ($x = 0.25$), the formation of S−S dimers opens a band gap, suggesting that the metallic-like band formation observed in disordered $Li_{2-\delta}TiS_3$ may be lost in this configuration. However, not all charge transfer

https://doi.org/10.1021/jacs.5c04018
J. Am. Chem. Soc. 2025, 147, 26238−26253

reactions are necessarily associated with dimer formation. It is plausible that regions supporting metallic-like band formation and electron delocalization persist via the formation of hole states that do not involve dimerization. Moreover, the formation of S−S dimers contributes to phase stability from a thermodynamic perspective, potentially facilitating smooth charge transfer reactions (Supporting Figure S7). Contrarily, isolated Li vacancies and holes are formed in ordered $\square_{0.5}Li_{1.5}TiS_3$, and thus local structural distortions are suppressed. Ordered Li_2TiS_3 is, therefore, electrochemically inactive, because of kinetic limitations. Note that S−S distances in ordered Li_2TiS_3 are ∼3.53 Å, which is much longer than that O−O distance (∼2.83 Å) in Li_2MnO_3. Hence, larger structural distortions are required to form S−S bonds in sulfide-based compounds. This finding is also consistent with the fact that the crystallinity is drastically lowered after Li extraction for disordered $Li_{2-x}TiS_3$ (Figures 3a and S3). Further Li removal and enrichment of vacant sites result in the structural distortion and formation of disulfide, trisulfide, and/or tetrasulfide ions for both phases, and thus the two PDOS are similar between disordered and ordered $\square LiTiS_3$ ($x = 0.5$).

CONCLUSIONS

Li-excess and stoichiometric metal sulfide systems are targeted as high-capacity electrode materials with anionic redox, and the activation mechanisms of anionic redox for these sulfide systems are systematically studied with different characterization methodologies and theoretical approach. These findings derived by joint theoretical and experimental study conclude that structural disordering with different local structures, including the unique environment of SLi_6 configuration formed only in the disordered structure, effectively activates anionic redox, which originates from high electronic conductivity associated with electron delocalization for sulfur 3p orbitals even without conductive d electrons coupled with easier structural distortion and S−S dimerization on delithiation. Although higher solubility to electrolyte solutions for the sulfide system is a practical problem as electrode materials, this problem is effectively mitigated by the use of highly concentrated electrolyte solutions, leading to a large reversible capacity, >300 mA h g^{-1}, with highly reversible anionic redox. The insights potentially result in the future development of high-energy and cost-effective electrode materials with the reversible redox reaction of anionic species used in host structures.

ASSOCIATED CONTENT

Supporting Information

The Supporting Information is available free of charge at https://pubs.acs.org/doi/10.1021/jacs.5c04018.

XRD patterns of precursors, CV data for powdered samples of rocksalt and layered Li_2TiS_3, original *in situ* XRD data of $Li_{2-x}TiS_3$, SEM/EDX data of fully charged $Li_{2-x}TiS_3$ with the disordered structure, reconstructed phase and absorption images, phase, XAS spectra, chemical state maps, edge-jumps, and normalized peak position and heights, obtained by X-ray ptychography for half-charged and fully charged $Li_{2-x}TiS_3$ with the disordered structure, DFT calculated voltage profile as a function of composition x in $Li_{2-x}TiS_3$, electron localization factors and density of states for ordered/disordered Li_2TiS_3 and disordered Li_2TiO_3, magnified views of the density of states (DOS) near the Fermi level for disordered $Li_{2-\delta}TiO_3$ and ordered/disordered $Li_{2-\delta}TiS_3$ with isosurface projections of charge density (PDF)

AUTHOR INFORMATION

Corresponding Author

Naoaki Yabuuchi − *Department of Chemistry and Life Science, Yokohama National University, Yokohama, Kanagawa 240-8501, Japan; Advanced Chemical Energy Research Center, Institute of Advanced Sciences, Yokohama National University, Yokohama, Kanagawa 240-8501, Japan;* orcid.org/0000-0002-9404-5693; Email: yabuuchi-naoaki-pw@ynu.ac.jp

Authors

Miyuki Shinoda − *Department of Chemistry and Life Science, Yokohama National University, Yokohama, Kanagawa 240-8501, Japan*

Koki Matsunoshita − *Department of Advanced Ceramics, Nagoya Institute of Technology, Nagoya, Aichi 466-8555, Japan*

Masanobu Nakayama − *Department of Advanced Ceramics, Nagoya Institute of Technology, Nagoya, Aichi 466-8555, Japan;* orcid.org/0000-0002-5113-053X

Satoshi Hiroi − *Faculty of Materials for Energy, Shimane University, Matsue, Shimane 690-8504, Japan;* orcid.org/0000-0001-5058-6757

Koji Ohara − *Faculty of Materials for Energy, Shimane University, Matsue, Shimane 690-8504, Japan; RIKEN SPring-8 Center, Sayo, Hyogo 679-5148, Japan; Research Center for Energy and Environmental Materials (GREEN), National Institute for Materials Science (NIMS), Tsukuba, Ibaraki 305-0044, Japan*

Masaki Abe − *RIKEN SPring-8 Center, Sayo, Hyogo 679-5148, Japan; International Center for Synchrotron Radiation Innovation Smart (SRIS), Tohoku University, Sendai, Miyagi 980-8577, Japan; Department of Metallurgy, Materials Science and Materials Processing, Graduate School of Engineering, Tohoku University, Sendai, Miyagi 980-8579, Japan; Institute of Multidisciplinary Research for Advanced Materials (IMRAM), Tohoku University, Sendai, Miyagi 980-8577, Japan;* orcid.org/0009-0002-1369-629X

Nozomu Ishiguro − *RIKEN SPring-8 Center, Sayo, Hyogo 679-5148, Japan; International Center for Synchrotron Radiation Innovation Smart (SRIS), Tohoku University, Sendai, Miyagi 980-8577, Japan;* orcid.org/0000-0003-3330-6236

Yukio Takahashi − *RIKEN SPring-8 Center, Sayo, Hyogo 679-5148, Japan; International Center for Synchrotron Radiation Innovation Smart (SRIS), Tohoku University, Sendai, Miyagi 980-8577, Japan; Institute of Multidisciplinary Research for Advanced Materials (IMRAM) and Institute for Materials Research, Tohoku University, Sendai, Miyagi 980-8577, Japan*

Gen Hasegawa − *Research Center for Energy and Environmental Materials (GREEN), National Institute for Materials Science (NIMS), Tsukuba, Ibaraki 305-0044, Japan;* orcid.org/0000-0002-9297-6902

Naoaki Kuwata − *Research Center for Energy and Environmental Materials (GREEN), National Institute for Materials Science (NIMS), Tsukuba, Ibaraki 305-0044, Japan;* orcid.org/0000-0002-0736-6967

https://doi.org/10.1021/jacs.5c04018
J. Am. Chem. Soc. 2025, 147, 26238−26253

Tsukasa Iwama − *Research Center for Energy and Environmental Materials (GREEN), National Institute for Materials Science (NIMS), Tsukuba, Ibaraki 305-0044, Japan; Graduate School of Chemical Sciences and Engineering, Hokkaido University, Sapporo, Hokkaido 060-0810, Japan*

Takuya Masuda − *Research Center for Energy and Environmental Materials (GREEN), National Institute for Materials Science (NIMS), Tsukuba, Ibaraki 305-0044, Japan; Graduate School of Chemical Sciences and Engineering, Hokkaido University, Sapporo, Hokkaido 060-0810, Japan;* orcid.org/0000-0001-7462-2177

Kosuke Suzuki − *Graduate School of Science and Technology, Gunma University, Kiryu, Gunma 376-8515, Japan*

Hirofumi Ishii − *National Synchrotron Radiation Research Center, Hsinchu 30076, Taiwan*

Yu-Cheng Shao − *National Synchrotron Radiation Research Center, Hsinchu 30076, Taiwan*

Daisuke Shibata − *SR Center, Ritsumeikan University, Kusatsu, Shiga 525-8577, Japan*

Akinori Irizawa − *SR Center, Ritsumeikan University, Kusatsu, Shiga 525-8577, Japan*

Toshiaki Ohta − *SR Center, Ritsumeikan University, Kusatsu, Shiga 525-8577, Japan*

Itsuki Konuma − *Department of Chemistry and Life Science, Yokohama National University, Yokohama, Kanagawa 240-8501, Japan*

Teppei Ohno − *Department of Chemistry and Life Science, Yokohama National University, Yokohama, Kanagawa 240-8501, Japan*

Yosuke Ugata − *Department of Chemistry and Life Science, Yokohama National University, Yokohama, Kanagawa 240-8501, Japan; Advanced Chemical Energy Research Center, Institute of Advanced Sciences, Yokohama National University, Yokohama, Kanagawa 240-8501, Japan;* orcid.org/0000-0002-8233-6725

Complete contact information is available at: https://pubs.acs.org/10.1021/jacs.5c04018

Notes

The authors declare no competing financial interest.

■ ACKNOWLEDGMENTS

N.Y. acknowledges the partial support from JSPS, Grant-in-Aid for Scientific Research (Grant Numbers 21H04698 and 24H02204). This work was partially supported by JST, CREST Grant Number JPMJCR21O6, Japan, and by MEXT Program: Data Creation and Utilization-Type Material Research and Development Project, Grant Number JPMXP1122712807. N.Y. acknowledges the partial support by JST as part of Adopting Sustainable Partnerships for Innovative Research Ecosystem (ASPIRE), Grant Number JPMJAP2313. This work was also partially supported by JST, Grant Number JPMJPF2016. K.O. thanks JSPS (Grant Number 19H05814). A part of this study was supported by JST, The Green Technologies for Excellence (GteX) Program, Grant Numbers JPMJGX23S3 and JPMJGX23S5. The synchrotron radiation experiments were performed at the BL04B2 of SPring-8 with the approval of the Japan Synchrotron Radiation Research Institute (JASRI) (Proposal No. 2023A1001). X-ray absorption work was done under the approval of the Photon Factory Program Advisory Committee (Proposal No. 2023G028). The X-ray spectroscopic ptychography experiments were performed on BL27SU at SPring-8 with the approval of the Japan Synchrotron Radiation Research Institute (Proposal No. 2021B1595). Thanks are extended to Prof. Hiroshi Sakurai for support in magnetization measurements.

■ REFERENCES

(1) Choi, J. U.; Voronina, N.; Sun, Y.-K.; Myung, S.-T. Recent Progress and Perspective of Advanced High-Energy Co-Less Ni-Rich Cathodes for Li-Ion Batteries: Yesterday, Today, and Tomorrow. *Adv. Energy Mater.* **2020**, *10*, No. 2002027.

(2) Li, H.; Cormier, M.; Zhang, N.; Inglis, J.; Li, J.; Dahn, J. R. Is Cobalt Needed in Ni-Rich Positive Electrode Materials for Lithium Ion Batteries? *J. Electrochem. Soc.* **2019**, *166*, A429−A439.

(3) Ikeda, N.; Konuma, I.; Rajendra, H. B.; Aida, T.; Yabuuchi, N. Why is the O3 to O1 phase transition hindered in LiNiO2 on full delithiation? *J. Mater. Chem. A* **2021**, *9*, 15963−15967.

(4) Konuma, I.; Ikeda, N.; Campéon, B. D. L.; Fujimura, H.; Kikkawa, J.; Luong, H. D.; Tateyama, Y.; Ugata, Y.; Yonemura, M.; Ishigaki, T.; Aida, T.; Yabuuchi, N. Unified understanding and mitigation of detrimental phase transition in cobalt-free LiNiO2. *Energy Storage Mater.* **2024**, *66*, No. 103200.

(5) Yabuuchi, N. Material Design Concept of Lithium-Excess Electrode Materials with Rocksalt-Related Structures for Rechargeable Non-Aqueous Batteries. *Chem. Rec.* **2019**, *19*, 690−707.

(6) Jacquet, Q.; Iadecola, A.; Saubanère, M.; Li, H.; Berg, E. J.; Rousse, G.; Cabana, J.; Doublet, M.-L.; Tarascon, J.-M. Charge Transfer Band Gap as an Indicator of Hysteresis in Li-Disordered Rock Salt Cathodes for Li-Ion Batteries. *J. Am. Chem. Soc.* **2019**, *141*, 11452−11464.

(7) Radin, M. D.; Vinckeviciute, J.; Seshadri, R.; Van der Ven, A. Manganese oxidation as the origin of the anomalous capacity of Mn-containing Li-excess cathode materials. *Nat. Energy* **2019**, *4*, 639−646.

(8) Kobayashi, Y.; Sawamura, M.; Kondo, S.; Harada, M.; Noda, Y.; Nakayama, M.; Kobayakawa, S.; Zhao, W.; Nakao, A.; Yasui, A.; Rajendra, H. B.; Yamanaka, K.; Ohta, T.; Yabuuchi, N. Activation and stabilization mechanisms of anionic redox for Li storage applications: Joint experimental and theoretical study on Li2TiO3−LiMnO2 binary system. *Mater. Today* **2020**, *37*, 43−55.

(9) Hansen, C. J.; Zak, J. J.; Martinolich, A. J.; Ko, J. S.; Bashian, N. H.; Kaboudvand, F.; Van der Ven, A.; Melot, B. C.; Nelson Weker, J.; See, K. A. Multielectron, Cation and Anion Redox in Lithium-Rich Iron Sulfide Cathodes. *J. Am. Chem. Soc.* **2020**, *142*, 6737−6749.

(10) Sakuda, A.; Takeuchi, T.; Okamura, K.; Kobayashi, H.; Sakaebe, H.; Tatsumi, K.; Ogumi, Z. Rock-salt-type lithium metal sulphides as novel positive-electrode materials. *Sci. Rep.* **2014**, *4*, No. 4883.

(11) Sakuda, A.; Ohara, K.; Kawaguchi, T.; Fukuda, K.; Nakanishi, K.; Arai, H.; Uchimoto, Y.; Ohta, T.; Matsubara, E.; Ogumi, Z.; Kuratani, K.; Kobayashi, H.; Shikano, M.; Takeuchi, T.; Sakaebe, H. A Reversible Rocksalt to Amorphous Phase Transition Involving Anion Redox. *Sci. Rep.* **2018**, *8*, No. 15086.

(12) Flamary-Mespoulie, F.; Boulineau, A.; Martinez, H.; Suchomel, M. R.; Delmas, C.; Pecquenard, B.; Le Cras, F. Lithium-rich layered titanium sulfides: Cobalt- and Nickel-free high capacity cathode materials for lithium-ion batteries. *Energy Storage Mater.* **2020**, *26*, 213−222.

(13) Jiang, Z.; Zhang, K.; Ding, Q.; Gao, C.; Zuo, Y.; Wang, H.; Cai, J.; Li, B.; Ai, X.; Xia, D. Metal−Ligand Spin-Lock Strategy for Inhibiting Anion Dimerization in Li-Rich Cathode Materials. *J. Am. Chem. Soc.* **2025**, *147*, 3062−3071.

(14) Marchandier, T.; Mariyappan, S.; Kirsanova, M. A.; Abakumov, A. M.; Rousse, G.; Foix, D.; Sougrati, M.-T.; Doublet, M. L.; Tarascon, J.-M. Triggering Anionic Redox Activity in Li3NbS4 Through Cationic Disordering or Substitution. *Adv. Energy Mater.* **2022**, *12*, No. 2201417.

(15) Shinoda, M.; Rajendra, H. B.; Yabuuchi, N. Rocksalt and Layered Metal Sulfides for Li Storage Applications: LiMe0.5Ti0.5S2 (Me = Fe2+, Mn2+, and Mg2+). *ACS Appl. Energy Mater.* **2022**, *5*, 2642−2646.
(16) Yabuuchi, N. Rational material design of Li-excess metal oxides with disordered rock salt structure. *Curr. Opin. Electrochem.* **2022**, *34*, No. 100978.
(17) Leube, B. T.; Robert, C.; Foix, D.; Porcheron, B.; Dedryvère, R.; Rousse, G.; Salager, E.; Cabelguen, P.-E.; Abakumov, A. M.; Vezin, H.; Doublet, M.-L.; Tarascon, J.-M. Activation of anionic redox in d0 transition metal chalcogenides by anion doping. *Nat. Commun.* **2021**, *12*, No. 5485.
(18) Ohara, K.; Tominaka, S.; Yamada, H.; Takahashi, M.; Yamaguchi, H.; Utsuno, F.; Umeki, T.; Yao, A.; Nakada, K.; Takemoto, M.; Hiroi, S.; Tsuji, N.; Wakihara, T. Time-resolved pair distribution function analysis of disordered materials on beamlines BL04B2 and BL08W at SPring-8. *J. Synchrot. Radiat.* **2018**, *25*, 1627−1633.
(19) Kresse, G.; Furthmuller, J. Efficiency of ab-initio total energy calculations for metals and semiconductors using a plane-wave basis set. *Comput. Mater. Sci.* **1996**, *6*, 15−50.
(20) Kresse, G.; Furthmüller, J. Efficient iterative schemes for ab initio total-energy calculations using a plane-wave basis set. *Phys. Rev. B* **1996**, *54*, 11169−11186.
(21) Perdew, J. P.; Burke, K.; Ernzerhof, M. Generalized gradient approximation made simple. *Phys. Rev. Lett.* **1996**, *77*, 3865−3868.
(22) Perdew, J. P.; Ruzsinszky, A.; Csonka, G. I.; Vydrov, O. A.; Scuseria, G. E.; Constantin, L. A.; Zhou, X.; Burke, K. Restoring the Density-Gradient Expansion for Exchange in Solids and Surfaces. *Phys. Rev. Lett.* **2008**, *100*, No. 136406.
(23) Blöchl, P. E. Projector augmented-wave method. *Phys. Rev. B* **1994**, *50*, 17935−17979.
(24) Sawamura, M.; Kobayakawa, S.; Kikkawa, J.; Sharma, N.; Goonetilleke, D.; Rawal, A.; Shimada, N.; Yamamoto, K.; Yamamoto, R.; Zhou, Y.; Uchimoto, Y.; Nakanishi, K.; Mitsuhara, K.; Ohara, K.; Park, J.; Byon, H. R.; Koga, H.; Okoshi, M.; Ohta, T.; Yabuuchi, N. Nanostructured LiMnO2 with Li3PO4 Integrated at the Atomic Scale for High-Energy Electrode Materials with Reversible Anionic Redox. *ACS Cent. Sci.* **2020**, *6*, 2326−2338.
(25) Kanno, A.; Ugata, Y.; Ikeuchi, I.; Hibino, M.; Nakura, K.; Miyaoka, Y.; Kawamura, I.; Shibata, D.; Ohta, T.; Yabuuchi, N. Durable Manganese-Based Li-Excess Electrode Material without Voltage Decay: Metastable and Nanosized Li2MnO1.5F1.5. *ACS Energy Lett.* **2023**, *8*, 2753−2761.
(26) Zhang, Y.; Ugata, Y.; Campéon, B. L.; Yabuuchi, N. Unlocking Electrode Performance of Disordered Rocksalt Oxides Through Structural Defect Engineering and Surface Stabilization with Concentrated Electrolyte. *Adv. Energy Mater.* **2024**, *14*, No. 2304074.
(27) Gao, B.; Jalem, R.; Tian, H.-K.; Tateyama, Y. Revealing Atomic-Scale Ionic Stability and Transport around Grain Boundaries of Garnet Li7La3Zr2O12 Solid Electrolyte. *Adv. Energy Mater.* **2022**, *12*, No. 2102151.
(28) Konuma, I.; Goonetilleke, D.; Sharma, N.; Miyuki, T.; Hiroi, S.; Ohara, K.; Yamakawa, Y.; Morino, Y.; Rajendra, H. B.; Ishigaki, T.; Yabuuchi, N. A near dimensionally invariable high-capacity positive electrode material. *Nat. Mater.* **2023**, *22*, 225−234.
(29) Ugata, Y.; Yabuuchi, N. New functionality of electrode materials with highly concentrated electrolytes. *Trends Chem.* **2023**, *5*, 672−683.
(30) Doi, T.; Shimizu, Y.; Matsumoto, R.; Hashinokuchi, M.; Inaba, M. Suppression of Mn−Ion-Dissolution of LiNi0.5Mn1.5O4 Electrodes in a Highly Concentrated Electrolyte Solution at Elevated Temperatures. *ChemistrySelect* **2017**, *2*, 8824−8827.
(31) Lee, J.; Urban, A.; Li, X.; Su, D.; Hautier, G.; Ceder, G. Unlocking the Potential of Cation-Disordered Oxides for Rechargeable Lithium Batteries. *Science* **2014**, *343*, 519−522.
(32) Suzuki, K.; Otsuka, Y.; Hoshi, K.; Sakurai, H.; Tsuji, N.; Yamamoto, K.; Yabuuchi, N.; Hafiz, H.; Orikasa, Y.; Uchimoto, Y.; Sakurai, Y.; Viswanathan, V.; Bansil, A.; Barbiellini, B. Magnetic Compton Scattering Study of Li-Rich Battery Materials. *Condens. Matter* **2022**, *7*, No. 4.
(33) Tsuchimoto, A.; Shi, X.-M.; Kawai, K.; Mortemard de Boisse, B.; Kikkawa, J.; Asakura, D.; Okubo, M.; Yamada, A. Nonpolarizing oxygen-redox capacity without O-O dimerization in Na2Mn3O7. *Nat. Commun.* **2021**, *12*, No. 631.
(34) Gorlin, Y.; Patel, M. U. M.; Freiberg, A.; He, Q.; Piana, M.; Tromp, M.; Gasteiger, H. A. Understanding the Charging Mechanism of Lithium-Sulfur Batteries Using Spatially Resolved Operando X-Ray Absorption Spectroscopy. *J. Electrochem. Soc.* **2016**, *163*, No. A930.
(35) Abe, M.; Kaneko, F.; Ishiguro, N.; Kubo, T.; Chujo, F.; Tamenori, Y.; Kishimoto, H.; Takahashi, Y. Visualization of Sulfur Chemical State of Cathode Active Materials for Lithium−Sulfur Batteries by Tender X-ray Spectroscopic Ptychography. *J. Phys. Chem. C* **2022**, *126*, 14047−14057.
(36) Abe, M.; Kaneko, F.; Ishiguro, N.; Kudo, T.; Matsumoto, T.; Hatsui, T.; Tamenori, Y.; Kishimoto, H.; Takahashi, Y. Development and application of a tender X-ray ptychographic coherent diffraction imaging system on BL27SU at SPring-8. *J. Synchrot. Radiat.* **2021**, *28*, 1610−1615.
(37) Mukai, K.; Yashima, M.; Hibino, K.; Terai, T. Experimental Visualization of Interstitialcy Diffusion of Li Ion in beta-Li2TiO3. *Acs Appl. Energ Mater.* **2019**, *2*, 5481−5489.
(38) Zunger, A.; Wei, S. H.; Ferreira, L. G.; Bernard, J. E. Special Quasirandom Structures. *Phys. Rev. Lett.* **1990**, *65*, 353−356.
(39) Lun, Z. Y.; Ouyang, B.; Cai, Z. J.; Clement, R.; Kwon, D. H.; Huang, J. P.; Papp, J. K.; Balasubramanian, M.; Tian, Y. S.; McCloskey, B. D.; Ji, H. W.; Kim, H.; Kitchaev, D. A.; Ceder, G. Design Principles for High-Capacity Mn-Based Cation-Disordered Rocksalt Cathodes. *Chem-Us* **2020**, *6*, 153−168.
(40) Yabuuchi, N.; Nakayama, M.; Takeuchi, M.; Komaba, S.; Hashimoto, Y.; Mukai, T.; Shiiba, H.; Sato, K.; Kobayashi, Y.; Nakao, A.; Yonemura, M.; Yamanaka, K.; Mitsuhara, K.; Ohta, T. Origin of Stabilization and Destabilization in Solid-State Redox Reaction of Oxide Ions for Rechargeable Lithium Batteries. *Nat. Commun.* **2016**, *7*, No. 13814.
(41) Tanibata, N.; Kondo, Y.; Yamada, S.; Maeda, M.; Takeda, H.; Nakayama, M.; Asaka, T.; Kitajou, A.; Okada, S. Nanotube-structured Na2V3O7 as a Cathode Material for Sodium-Ion Batteries with High-rate and Stable Cycle Performances. *Sci. Rep-Uk* **2018**, *8*, No. 17199.
(42) Sato, K.; Nakayama, M.; Glushenkov, A. M.; Mukai, T.; Hashimoto, Y.; Yamanaka, K.; Yoshimura, M.; Ohta, T.; Yabuuchi, N. Na-Excess Cation-Disordered Rocksalt Oxide: Na1.3Nb0.3Mn0.4O2. *Chem. Mater.* **2017**, *29*, 5043−5047.
(43) Nakayama, M.; Nishii, K.; Watanabe, K.; Tanibata, N.; Takeda, H.; Itoh, T.; Asaka, T. First-principles study of the morphology and surface structure of LaCoO3 and La0.5Sr0.5Fe0.5Co0.5O3 perovskites as air electrodes for solid oxide fuel cells. *Sci. Technol. Adv. Mater.:Methods* **2021**, *1*, 24−33.
(44) Pantelides, S. T.; Mickish, D. J.; Kunz, A. B. Electronic structure and properties of magnesium oxide. *Phys. Rev. B* **1974**, *10*, 5203−5212.
(45) Ke, X. Z.; Tanaka, I. Atomistic mechanism of proton conduction in solid CsHSO4 by a first-principles study. *Phys. Rev. B* **2004**, *69*, No. 165114.
(46) Seo, D. H.; Lee, J.; Urban, A.; Malik, R.; Kang, S.; Ceder, G. The structural and chemical origin of the oxygen redox activity in layered and cation-disordered Li-excess cathode materials. *Nat. Chem.* **2016**, *8*, 692−697.
(47) Kobayashi, Y.; Sawamura, M.; Kondo, S.; Harada, M.; Noda, Y.; Nakayama, M.; Kobayakawa, S.; Zhao, W. W.; Nakao, A.; Yasui, A.; Rajendra, H. B.; Yamanaka, K.; Ohta, T.; Yabuuchi, N. Activation and stabilization mechanisms of anionic redox for Li storage applications: Joint experimental and theoretical study on Li2TiO3-LiMnO2 binary system. *Mater. Today* **2020**, *37*, 43−55.
(48) Cococcioni, M.; Marzari, N. Energetics and cathode voltages of LiMPO4 olivines (M = Fe, Mn) from extended Hubbard functionals. *Phys. Rev. Mater.* **2019**, *3*, No. 033801.

https://doi.org/10.1021/jacs.5c04018
J. Am. Chem. Soc. 2025, 147, 26238−26253

(49) Urban, A.; Seo, D.-H.; Ceder, G. Computational understanding of Li-ion batteries. *npj Comput. Mater.* **2016**, *2*, No. 16002.
(50) Maxisch, T.; Zhou, F.; Ceder, G. Ab initio study of the migration of small polarons in olivine LiFePO4 and their association with lithium ions and vacancies. *Phys. Rev. B* **2006**, *73*, No. 104301.
(51) Kong, F.; Longo, R. C.; Park, M.-S.; Yoon, J.; Yeon, D.-H.; Park, J.-H.; Wang, W.-H.; Kc, S.; Doo, S.-G.; Cho, K. Ab initio study of doping effects on LiMnO2 and Li2MnO3 cathode materials for Li-ion batteries. *J. Mater. Chem. A* **2015**, *3*, 8489−8500.
(52) Lee, E.; Lee, D.-H.; Bessette, S.; Park, S.-W.; Brodusch, N.; Lazaris, G.; Kim, H.; Malik, R.; Gauvin, R.; Seo, D.-H.; Lee, J. Nearly all-active-material cathodes free of nickel and cobalt for Li-ion batteries. *Energy Environ. Sci.* **2024**, *17*, 3753−3764.

https://doi.org/10.1021/jacs.5c04018
J. Am. Chem. Soc. 2025, 147, 26238−26253